Development of a depth-resolved x-ray magnetic circular dichroism: application to Fe/Cu(100) ultrathin films

2003 J. Phys.: Condens. Matter 15 S561

(http://iopscience.iop.org/0953-8984/15/5/310)

INSTITUTE OF PHYSICS PUBLISHING JOURNAL OF PHYSICS: CONDENSED MATTER

J. Phys.: Condens. Matter **15** (2003) S561–S571 PII: S0953-8984(03)55907-0

Development of a depth-resolved x-ray magnetic circular dichroism: application to Fe/Cu(100) ultrathin films

Kenta Amemiya[1], **Soichiro Kitagawa**[1], **Daiju Matsumura**[1], **Toshihiko Yokoyama**[2] **and Toshiaki Ohta**[1,3]

[1] Department of Chemistry, Graduate School of Science, The University of Tokyo, Hongo, Bunkyo-ku, Tokyo 113-0033, Japan
[2] Institute for Molecular Science, Myodaiji-cho, Okazaki, Aichi 444-8585, Japan

E-mail: ohta@chem.s.u-tokyo.ac.jp

Received 11 November 2002
Published 27 January 2003
Online at stacks.iop.org/JPhysCM/15/S561

Abstract

A depth-resolved technique is applied in the x-ray magnetic circular dichroism (XMCD) method by controlling the probing depth of the electron yield XMCD spectra. The usefulness of this technique is demonstrated for the study of magnetic structures of 4 and 8 ML Fe films grown on Cu(100), which are known to exhibit peculiar magnetic depth profiles. It was directly shown that the 4 ML film is uniformly magnetized, while the magnetic moment is localized at the surface in the case of the 8 ML film. The XMCD spectrum for each layer of the 4 ML film was separately extracted. All the extracted spectra were almost identical to each other, confirming the ferromagnetic coupling over the whole film. As for the 8 ML film, it was suggested that the surface two layers are ferromagnetically coupled, while the inner layers are in a spin density wave state with a wavenumber $q = 2\pi/2.4d$.

1. Introduction

Magnetic thin films often show peculiar magnetic properties such as enhancement of the magnetic moment and large magnetic anisotropy, especially at the surface and interface [1–13]. Moreover, surface magnetism plays an important role when the thin film is exposed to various gases such as CO and oxygen [12–17]. In the case of H or CO adsorption on a Ni/Cu(100) film, the magnetic easy axis rotates from the surface parallel direction to the surface normal [12, 13]. The extraction of the surface magnetic property is necessary if one wishes to understand so drastic a phase transition. So far, the surface and interface magnetic

[3] Author to whom any correspondence should be addressed.

0953-8984/03/050561+11$30.00

properties have been investigated mostly by changing the film thickness, using total magnetic moment measurements such as magneto-optical Kerr effect (MOKE) ones. Therefore, it has been necessary to assume that the magnetic properties at the surface, interface, and inner layers are unchanged regardless of the film thickness. Such an assumption is not always justified, however, since the ultrathin film is subject to changes in the geometrical and electronic environments as the thickness changes.

Some attempts have been made to directly determine the surface and interface magnetic properties of ultrathin films without changing the film thickness. Spin-polarized appearance potential spectroscopy (SP-APS) has been developed to study surface magnetization owing to the short attenuation length of electrons, though the interpretation of the spectrum obtained is still unclear [18–20]. Another powerful tool is the magnetization-induced second-harmonic generation (MSHG) [21–23], which is intrinsically surface sensitive. However, the magnetic properties of the inner layers cannot be investigated with this method. A depth-resolved technique, which can directly and qualitatively determine the magnetic depth profile of the whole film, has thus been desired for a long time.

The x-ray magnetic circular dichroism (XMCD) method has been well established as one of the most suitable techniques for investigating various magnetic materials, because it has element selectivity and the spin and orbital magnetic moments can be quantitatively determined by using the sum rules [24, 25]. Therefore it is quite advantageous if the XMCD is combined with a depth-resolved technique. Recently, a depth-resolved XMCD measurement was reported which utilizes the x-ray standing wave method [9]. It requires, however, a multilayer interference structure under the ultrathin film sample in order to generate standing waves. The application of this technique is thus restricted.

In the present paper, we demonstrate a novel depth-resolved XMCD technique, which can be generally applied to ordinary ultrathin film samples. In this new technique, the electron yield XMCD spectra were measured with various probing depths by changing the electron detection angles. The magnetic depth profile was determined by fitting a series of spectra, taking the electron attenuation length into account. This method has been applied to the Fe/Cu(100) ultrathin films, which has been one of the most controversial and the most widely investigated systems over the last decade [18, 20, 23, 26–35].

For the Fe/Cu(100) ultrathin films, most of the previous studies unanimously remark that the film takes the ferromagnetic (FM) face-centred-tetragonal (fct) structure below $\sim$4 ML (region I) and the body-centred-cubic (bcc) one beyond $\sim$12 ML (region III). In the case of 5–11 ML film (region II), the film is believed to show a face-centred-cubic (fcc) structure covered with fct surface layers. The total magnetic moment in this region stays almost constant regardless of the film thickness, and is comparable to that for a FM 2 ML film. Since CO exposure lowers the Curie temperature of the film [26], it has been supposed that only the top two surface layers are ferromagnetically coupled. This model has been verified more directly by SP-APS and MSHG experiments [18, 23], owing to their surface sensitivity.

As for the inner layers, a collinear antiferromagnetic state was proposed, because the total magnetic moment slightly oscillates as a function of film thickness [27, 28]. The previous *ab initio* calculations also assumed collinear spin states, whereas the magnetic structure of a fcc Fe particle in a Cu matrix has been determined to be an antiferromagnetic incommensurate spin density wave (SDW) [29–32]. In contrast, recent careful MOKE measurements [33] indicated a SDW state with a wavenumber $q = 2\pi/2.7d$ for the inner layers. Here, d denotes the interlayer distance of the film. The aim of our study is to directly clarify this controversial magnetic depth profile of the Fe/Cu(100) films by using the newly developed depth-resolved XMCD technique.

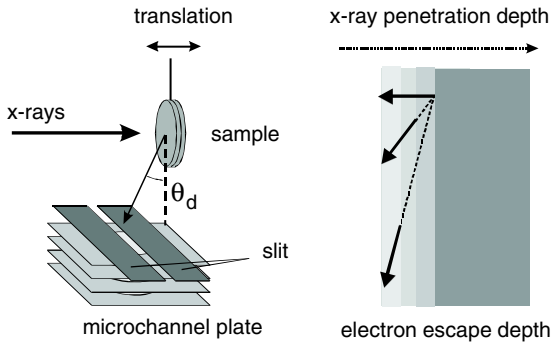

Figure 1. The schematic layout for depth-resolved XMCD measurements at normal x-ray incidence. The electron detection angle θ_d can be altered by translating a sample along the incident x-ray beam. As the angle θ_d decreases, the electron escape depth decreases as shown in the figure on the right.

2. Experiment

A layout for depth-resolved XMCD measurements at normal x-ray incidence is depicted schematically in figure 1. Since all the Fe/Cu(100) films that we investigated (regions I and II only) are known to have perpendicular magnetic anisotropy, all the spectra were taken at normal x-ray incidence. The acceptance angle of a microchannel plate detector was restricted to $\sim 5^\circ$ by a slit. A sample was translated along the incident x-ray beam in order to change the detection angle θ_d for emitted electrons. Therefore, the probing depth was controlled by changing the sample position. A partial electron yield mode with a retarding voltage of -500 V was adopted to enhance surface sensitivity. Care was taken to ensure that no component around the sample obstructs the emitted electrons, in order to maintain the depth resolution. The sample was magnetized by a current pulse through a coil, and then the coil was retracted by ~ 50 mm during the measurement. Accordingly, only the remnant magnetization was investigated.

All the experiments were performed at the soft-x-ray station, BL-7A, in the Photon Factory [36]. Circularly polarized x-rays (circular polarization factor $P_c \sim 0.8$) were obtained by collecting light from either above (+0.4 mrad) or below (-0.4 mrad) the orbit plane of the storage ring. The energy resolution around the Fe L edge was ~ 1 eV with the photon flux of $\sim 2 \times 10^{10}$ photons s^{-1}. A clean and ordered Cu(100) single crystal was prepared by repeated cycles of Ar^+ bombardment (1.5 kV) and annealing to ~ 900 K. The cleanliness and order of the surface were checked with NEXAFS (near-edge x-ray absorption fine-structure) and LEED (low-energy electron diffraction) observations. Fe was deposited on the clean surface at room temperature by electron bombardment heating of an Fe rod. Since the thickness of the film is critical for the depth-resolved XMCD analyses, the film thickness was monitored by an *in situ* RHEED (reflection high-energy electron diffraction) observation during the film growth. No additional Fe deposition was performed after the XMCD measurement, in order to ensure that the film thickness was determined precisely and to avoid surface contamination with residual gases. The XMCD spectra were recorded at ~ 110 K by changing the sample magnetization or the x-ray helicity.

3. Results and discussion

Figure 2 shows Fe and Cu L-edge x-ray absorption spectra for an 8 ML Fe film taken with various electron detection angles, θ_d. Here, θ_d is defined as an angle from the sample surface.

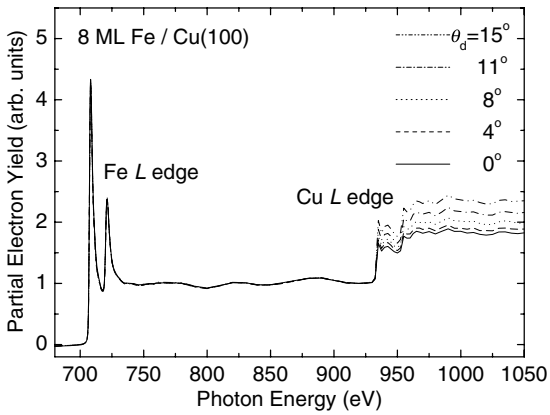

Figure 2. Fe and Cu L-edge x-ray absorption spectra for an 8 ML Fe film grown on Cu(100) taken with electron detection angles, θ_d, of 0 (surface parallel direction), 4°, 8°, 11°, and 15°. Each spectrum is normalized to the Fe edge jump after subtraction of a linear pre-edge background.

Each spectrum was obtained by subtraction of a linear pre-edge background and subsequent normalization at 740 eV. One can clearly see that the Cu/Fe edge jump ratio becomes larger as θ_d increases, confirming that the surface parallel detection ($\theta_d = 0°$) is the most surface sensitive and that the probing depth becomes larger with increasing θ_d. Unfortunately, the probing depth is not expected to be proportional to $\sin\theta_d$, mainly because of the inelastic scattering process of the emitted electrons. This is inevitably a problem as long as one adopts the partial electron yield detection, where the electrons with various kinetic energies are collected. There is a great advantage of this detection mode, however: the electron diffraction effect is negligible, because the kinetic energy range for the collected electrons is so wide. The electron diffraction effect is further diminished because the slit on the detector does not restrict the azimuthal angle of the emitted electrons.

In order to estimate the probing depth experimentally, the Fe edge jump intensity was plotted as a function of film thickness in figure 3. Here, the Fe edge jump intensity was estimated at 740 eV, after multiplication by a factor to make the intensity at the pre-edge energy (700 eV in the present study) unity, and subsequent subtraction of a background spectrum, which was obtained from the bare Cu(100) surface. Note that the edge jump would be proportional to the film thickness if the probing depth were infinity. The observed values saturate as the thickness increases, however, due to the finite probing depth. Moreover, the deviation from linearity is most prominent for $\theta_d = 0°$, indicating that the 0° detection is the most surface sensitive. We estimated the probing depth, λ, for each detection angle, θ_d, by fitting the Fe edge jump intensity assuming an exponential decay of the emitted electrons. In the fitting process, self-absorption of the incident x-rays was also taken into consideration. The estimated probing depth, λ, varies from $2.1d$ to $3.9d$ as indicated in figure 3.

Figure 4 shows XMCD spectra for 4 and 8 ML Fe films (regions I and II, respectively) taken with various detection angles, θ_d. All the spectra for the 4 ML film show almost identical XMCD intensities regardless of θ_d, suggesting that the whole film is uniformly magnetized. In contrast, the XMCD signal from the 8 ML film is drastically reduced as λ increases. Moreover, the XMCD intensity for the 8 ML film is more than two times smaller than those for the 4 ML film. Therefore, it was directly concluded that the magnetic moment in the 8 ML film is localized around the surface. In order to clarify the magnetic depth profile, we performed curve fitting analyses using a series of XMCD spectra taken at $\theta_d = 0°$, 4°, 8°, 12°, and 15°.

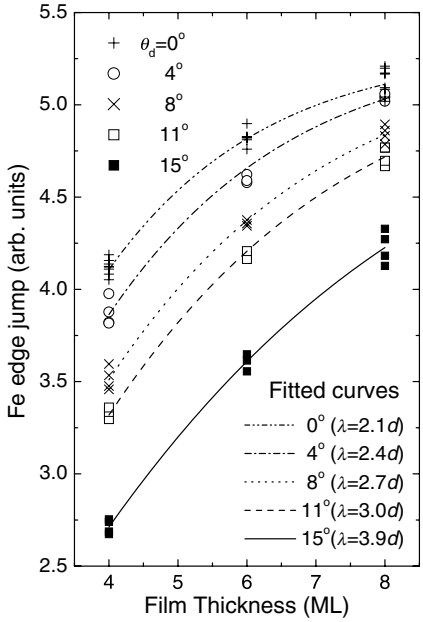

Figure 3. Fe L-edge jump intensity as a function of film thickness, together with the fitted curves assuming an exponential decay for the emitted electrons. λ indicates the estimated probing depth for each electron detection angle, θ_d.

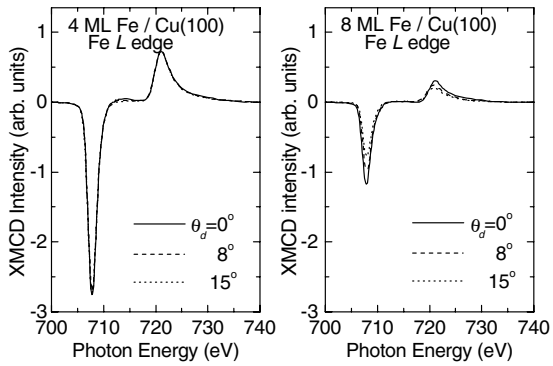

Figure 4. Fe L-edge XMCD spectra for 4 and 8 ML Fe films grown on Cu(100) taken with electron detection angles, θ_d, of 0 (surface parallel direction), 8°, and 15°.

As for the 4 ML film, the XMCD spectrum for each layer was extracted as shown in figure 5, by simulating the observed spectra using the estimated probing depth, λ (see the appendix for the details). Again, an exponential decay of the emitted electrons was assumed and self-absorption of incident x-rays was taken into consideration. The extracted spectra for each of the layers are essentially identical, confirming the uniform magnetization. In the case of the 8 ML film (region II), which is of most interest, the extraction of the XMCD spectrum for each layer is impossible because of there being too many layers. Therefore, we firstly divided the film into the surface and inner regions (two and six layers thick, respectively), assuming that all the Fe atoms in each region have the same magnetic moment. The extracted XMCD spectra

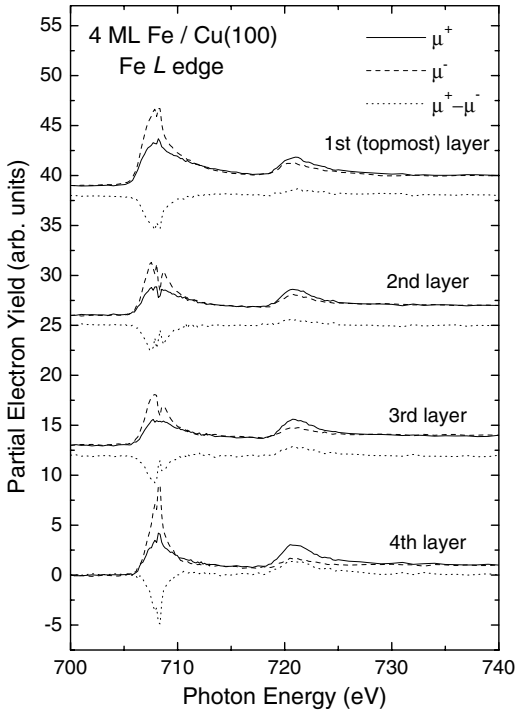

Figure 5. Extracted Fe L-edge circularly polarized (solid and dashed curves) and XMCD (dotted curve) spectra for each layer of a 4 ML Fe film.

are depicted in figure 6, which apparently shows that the surface region is ferromagnetically coupled while the inner one has almost no magnetic moment on average.

In order to further investigate the magnetic depth profile of the inner layers, we next assumed that the surface region is ferromagnetically coupled while the inner one is in a SDW state with wavenumber q. Here, the thickness of the surface FM region is assumed to be N_{F} layers. In this case, the XMCD intensity, M_n, for the nth layer from the surface is expressed by

$$M_n(E) = M_{\mathrm{FM}}(E) \qquad (n \leqslant N_{\mathrm{F}}), \tag{1}$$

$$M_n(E) = M_{\mathrm{SDW}}(E)\cos[q(n - n_0)d] \qquad (n \geqslant N_{\mathrm{F}} + 1), \tag{2}$$

where E is the photon energy and $n_0 = N_{\mathrm{F}} + 1$ (the first layer of the SDW region). The following variables were used as fitting parameters:

(a) XMCD spectra, $M_{\mathrm{FM}}(E)$ and $M_{\mathrm{SDW}}(E)$, for the FM and SDW (at $n = n_0$) regions, respectively,
(b) the SDW wavenumber, q (the examined range was 0, $2\pi/8d$–$2\pi/2d$), and
(c) thickness of the surface FM region, N_{F} (=1, 2).

By adopting these general expressions, the FM and collinear antiferromagnetic states (corresponding to $q = 0$ and $2\pi/2d$, respectively) for the inner region are also included in the analyses, as well as the nonmagnetic one ($M_{\mathrm{SDW}} = 0$). For instance, the above-mentioned simple two-region model, which led to figure 6, corresponds to $N_{\mathrm{F}} = 2$ and $q = 0$. Note here that the magnetic coupling at the FM/SDW interface is FM if $M_{\mathrm{FM}}(E)$ and $M_{\mathrm{SDW}}(E)$ have the same sign, and vice versa.

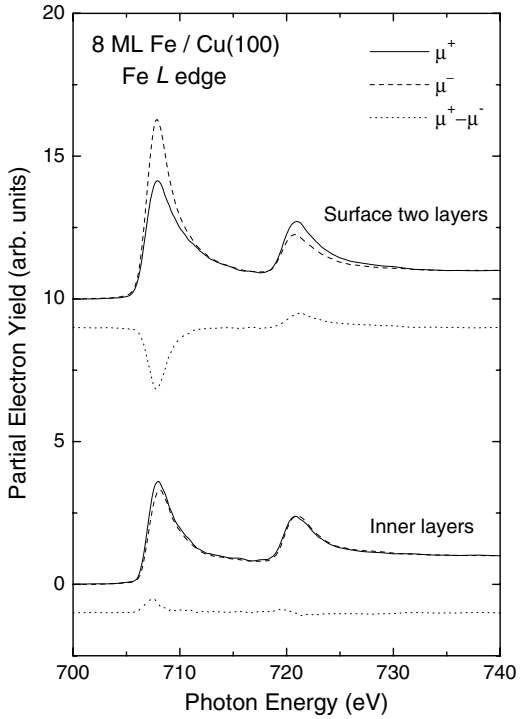

Figure 6. Extracted Fe L-edge circularly polarized (solid and dashed curves) and XMCD (dotted curve) spectra for surface (two-layer-thick) and inner (six-layer-thick) regions of an 8 ML film. It was assumed that all the Fe atoms in each region have the same magnetic moment.

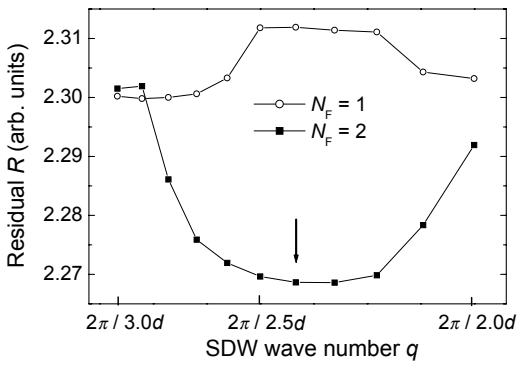

Figure 7. Residual, R (see the appendix for the definition), between the observed and simulated spectra as a function of wavenumber, q, with $N_{\mathrm{F}} = 1$ (open circles) and 2 (filled squares). All the fitting parameters other than q and N_{F} are optimized at each point.

We then optimized the above parameters to minimize the difference between the observed and simulated spectra (see the appendix), yielding $q = 2\pi/2.4d$ and $N_{\mathrm{F}} = 2$. The minimized residual, R (see the appendix for the definition), at each q and N_{F}, is plotted in figure 7 around $q = 2\pi/2.4d$. One can see that the collinear antiferromagnetic coupling ($q = 2\pi/2d$) is unlikely to be adopted. The extracted XMCD spectra, $M_{\mathrm{FM}}(E)$ and $M_{\mathrm{SDW}}(E)$, are depicted in figure 8. It should be emphasized that the sign of the XMCD spectrum for the first layer of the

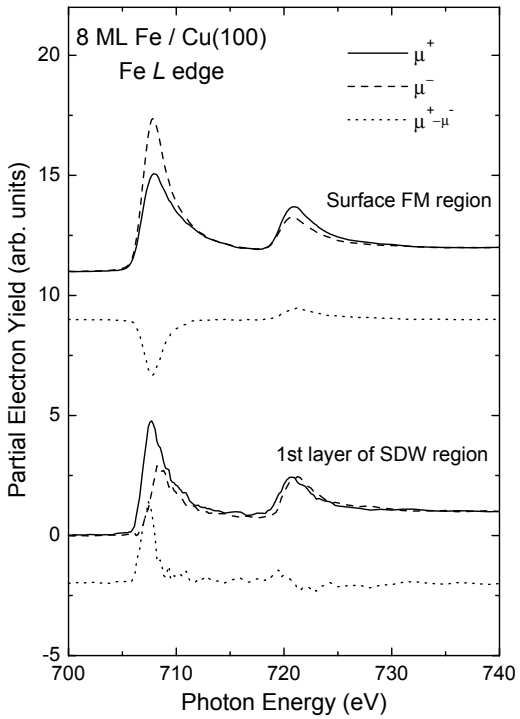

Figure 8. Extracted Fe L-edge circularly polarized (solid and dashed curves) and XMCD (dotted curve) spectra for the surface FM and inner SDW regions of an 8 ML Fe film with the optimized SDW wavenumber ($q = 2\pi/2.4d$) and FM layer thickness ($N_F = 2$). For the SDW region, only the spectrum for the first layer (the third layer from the surface) is given.

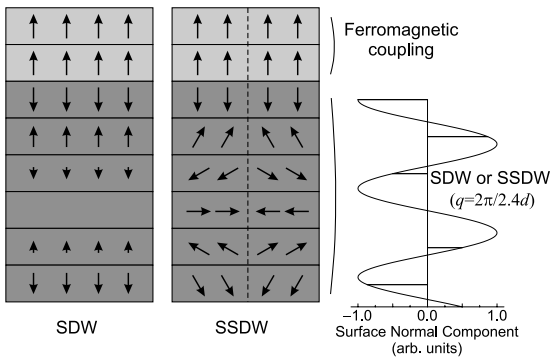

Figure 9. The magnetic structure model for the 8 ML Fe film grown on Cu(100). Arrows indicate the size and direction of the magnetic moment. A dashed line in the SSDW state indicates the domain boundary.

SDW region is opposite to that for the surface FM layers, indicating an antiferromagnetic FM/SDW interface coupling. Moreover, the XMCD intensity for the SDW region is comparable to that for the surface layers as well as those for the 4 ML film (figure 5). It was thus suggested that the SDW amplitude is as large as the magnetic moment in the FM Fe film.

The magnetic structure model obtained is schematically illustrated in figure 9. It should be remarked here that a spiral spin density wave (SSDW) cannot be excluded because the

in-plane magnetic structure is intrinsically undetectable with our experiments. In the case of a SSDW state, the size of the Fe magnetic moment for each layer is unchanged but rotates, as depicted in figure 9. Therefore, the surface normal component of the magnetic moment in the SSDW state is just the same as that of the normal SDW, where only the size (and sign) of the magnetic moment changes. Note that even a grazing-incidence XMCD measurement cannot distinguish the SSDW from the normal SDW, because the in-plane magnetic components in the SSDW state should cancel out within each layer due to the domain formation as shown in figure 9. Therefore, we have observed just the surface normal component of the Fe magnetic moment in either the SDW or SSDW state.

4. Conclusions

It has been shown that the probing depth of the electron yield XMCD spectra is controlled by changing the detection angles for the emitted electrons. Based on this, a depth-resolved XMCD technique has been developed by measuring the XMCD spectra with various probing depths. This novel technique was applied to the 4 ML (region I) and 8 ML (region II) Fe films grown on Cu(100), which exhibit peculiar magnetic depth profiles. It was directly shown that the 4 ML film is uniformly magnetized, while the magnetic moment is localized around the surface in the case of the 8 ML film. The XMCD spectra for each of the layers of the 4 ML film were separately extracted; they all show the same sign and similar intensities. A FM coupling in region I is thus confirmed. As for the 8 ML film, it was suggested that the top two surface layers are ferromagnetically coupled, while the inner layers are in a SDW state with a wavenumber $q = 2\pi/2.4d$. The extracted XMCD indicated that the SDW amplitude is comparable to the magnetic moment in the FM Fe, and that the FM/SDW interface coupling is antiferromagnetic. It should be noted, however, that the possibility of a SSDW for the inner region cannot be excluded, because such an in-plane magnetic structure is undetectable with the XMCD measurements.

This new technique can be easily applied to in-plane magnetization cases (with grazing x-ray incidence), by rotating the slit above the detector and changing the relative position of the sample and slit appropriately. It becomes a bit complicated, however, to control the probing depth in this configuration. As a future project, we are planning to remove the slit and utilize an imaging-type microchannel plate detector. A series of XMCD spectra with various probing depths will be obtained simultaneously without changing the sample position, drastically reducing the data acquisition time. In addition, both the normal-and grazing-x-ray-incidence spectra will be recorded by simply rotating the sample without changing any other configurations.

Acknowledgments

The present work was performed with the approval of the Photon Factory Programme Advisory Committee (PF-PAC Nos 2001S2-003, 2001G013). The authors are grateful for the financial support of Grants-in-Aid for Scientific Research (Nos 13740390, 10304059, 12440193, 14204069).

Appendix. The expression for the depth-resolved XMCD spectra

In this appendix the expression for the depth-resolved XMCD spectra is derived, by assuming an exponential decay for the emitted electrons. The electron diffraction effects are neglected

because the electrons with various kinetic energies are collected and the slit on the detector does not restrict the azimuthal angle of the emitted electrons. Due to the self-absorption effect, the intensity of the incident x-rays, $I_n^0(E)$, at the nth layer from the surface is expressed as

$$I_n^0(E) = I^0(E)\exp\left[\frac{-d}{\cos\theta}\sum_{k=1}^{n-1}\mu_k(E)\right], \tag{A.1}$$

where $\mu_k(E)$ is the absorption coefficient for the kth layer, θ the x-ray incidence angle to the surface normal, and $I^0(E)$ the original x-ray intensity. Since the electrons emitted from each layer of the film are attenuated by the upper layers, the electron yield is given as follows:

$$Y_n(E) = CI_0(E)\mu_n(E)\exp\left[\frac{-d}{\cos\theta}\sum_{k=1}^{n-1}\mu_k(E)\right]\exp\left[\frac{-d(n-1)}{\lambda}\right], \tag{A.2}$$

where $Y_n(E)$ represents the number of the detected electrons which are emitted from the nth layer, C the detection efficiency, and λ the probing depth.

Accordingly, the total number of detected electrons for the circularly polarized x-rays, $Y^{\pm}(E)$, normalized by the original x-ray intensity, $I^0(E)$, is given by

$$Y^{\pm}(E) = C\sum_{n=1}^{N}\mu_n^{\pm}(E)\exp\left[-d\left\{\frac{n-1}{\lambda}+\frac{1}{\cos\theta}\sum_{k=1}^{n-1}\mu_k^{\pm}(E)\right\}\right], \tag{A.3}$$

where N is the total number of layers, and $\mu_n^{\pm}(E)$ is the absorption coefficient for the circularly polarized x-rays for the nth layer. One can extract the circularly polarized spectrum, $\mu_n^{\pm}(E)$, by optimizing $\mu_n^{\pm}(E)$ such that the residual,

$$R^{\pm}(E) = \sum_m (Y_m^{\pm\mathrm{ex}}(E) - Y_m^{\pm\mathrm{sim}}(E))^2 \tag{A.4}$$

becomes a minimum. Here, $Y_m^{\pm\mathrm{ex}}(E)$ is the observed electron yield spectrum taken with the probing depth λ_m, and $Y_m^{\pm\mathrm{sim}}(E)$ is the simulated spectrum given by substituting λ_m for λ in equation (A.3). Note that $Y_m^{\pm\mathrm{ex}}(E)$ should be normalized such that $Y_m^{\pm\mathrm{ex}}(E) = Y_m^{\pm\mathrm{sim}}(E)$ at the pre- and post-edge energies ($E_{\mathrm{pre}} = 700$ eV and $E_{\mathrm{post}} = 740$ eV in the present study, respectively), where $\mu_n^{\pm}(E_{\mathrm{pre}})$ and $\mu_n^{\pm}(E_{\mathrm{post}})$ are supposed to be identical to the reported absorption coefficients for the bulk material. The XMCD spectrum, $M_n(E)$, for the nth layer is thus obtained from

$$M_n(E) = \mu_n^{+}(E) - \mu_n^{-}(E). \tag{A.5}$$

In order to ensure the reliability of the analyses, we did not use any reference spectrum in the fitting process. Moreover, we optimized $\mu_n^{+}(E)$ and $\mu_n^{-}(E)$ independently at each photon energy. That is, $M_n(E)$ was extracted by a purely mathematical procedure.

In the case of the SDW state, $\mu_n^{+}(E)$ and $\mu_n^{-}(E)$ cannot be separately extracted because the $M_n(E)$ are restricted as given in equation (2). Therefore, we introduced $A_n(E)$, which is defined by

$$A_n(E) = (\mu_n^{+}(E) + \mu_n^{-}(E))/2, \tag{A.6}$$

and assumed that

$$A_n(E) = A_{\mathrm{FM}}(E) \qquad (n \leqslant N_{\mathrm{F}}), \tag{A.7}$$

$$A_n(E) = A_{\mathrm{SDW}}(E) \qquad (n \geqslant N_{\mathrm{F}}+1). \tag{A.8}$$

Then $M_{\mathrm{FM}}(E)$, $A_{\mathrm{FM}}(E)$, $M_{\mathrm{SDW}}(E)$, and $A_{\mathrm{SDW}}(E)$ were similarly optimized for each q and N_{F} to minimize the residual, $R(E)$, which is defined by

$$R(E) = \sum_m (Y_m^{+\mathrm{ex}}(E) - Y_m^{+\mathrm{sim}}(E))^2 + \sum_m (Y_m^{-\mathrm{ex}}(E) - Y_m^{-\mathrm{sim}}(E))^2. \tag{A.9}$$

Finally, the total residual, R, is given by

$$R = \int R(E)\,\mathrm{d}E \tag{A.10}$$

which is plotted in figure 7 as a function of q and N_F.

References

[1] Tischer M, Hjortstam O, Arvanitis D, Dunn J H, May F, Baberschke K, Trygg J, Wills J M, Johansson B and Eriksson O 1995 *Phys. Rev. Lett.* **75** 1602
[2] Wu Y, Stöhr J, Hermsmeier B D, Samant M G and Weller D 1992 *Phys. Rev. Lett.* **69** 230
[3] Weller D, Wu Y, Stöhr J, Samant M G, Hermsmeier B D and Chappert C 1994 *Phys. Rev.* B **49** 12888
[4] Nakajima N, Koide T, Shidara T, Miyauchi H, Fukutani H, Fujimori A, Iio K, Katayama T, Nývlt M and Suzuki M 1998 *Phys. Rev. Lett.* **81** 5229
[5] Tatnall C J, Schille J P, Grundy P J and Lord D G 1997 *J. Magn. Magn. Mater.* **165** 391
[6] Dürr H A, Dhesi S S, Dudzik E, Knabben D, van der Laan G, Goedkoop J B and Hillebrecht F U 1999 *Phys. Rev.* B **59** R701
[7] Engel B N, Wiedmann M H, Leeuwen R A V and Falco C M 1993 *J. Magn. Magn. Mater.* **126** 532
[8] Koide T, Miyauchi H, Okamoto J, Shidara T, Fujimori A, Amemiya K, Takeshita H, Yuasa S, Katayama T and Suzuki Y 2001 *Phys. Rev. Lett.* **87** 257201
[9] Kim S-K and Kortright J B 2001 *Phys. Rev. Lett.* **86** 1347
[10] López-Urías F, Dorantes-Dávila J and Dreyssé H 1997 *J. Magn. Magn. Mater.* **165** 262
[11] Szunyogh L, Újfalussy B, Bruno P and Weinberger P 1997 *J. Magn. Magn. Mater.* **165** 254
[12] Vollmer R, Gutjahr-Loser Th, Kirschner J, van Dijken S and Poelsema B 1999 *Phys. Rev.* B **60** 6277
[13] van Dijken S, Vollmer R, Poelsema B and Kirschner J 2000 *J. Magn. Magn. Mater.* **210** 316
[14] Chubb S R and Pickett W E 1987 *Phys. Rev. Lett.* **58** 1248
[15] Wu R and Freeman A J 1992 *Phys. Rev.* B **45** 7532
[16] May F, Tischer M, Arvanitis D, Russo M, Dunn J H, Henneken H, Wende H, Chauvistré R, Mårtensson N and Baberschke K 1996 *Phys. Rev.* B **53** 1076
[17] Matsumura D, Yokoyama T, Amemiya K, Kitagawa S and Ohta T 2002 *Phys. Rev.* B **66** 024402
[18] Detzel Th, Vonbank M, Donath M and Dose V 1995 *J. Magn. Magn. Mater.* **147** L1
[19] Rangelov G, Kang H D, Reinmuth J and Donath M 2000 *Phys. Rev.* B **61** 549
[20] Popescu V, Ebert H, Szunyogh L, Weinberger P and Donath M 2000 *Phys. Rev.* B **61** 15241
[21] Reif J, Zink J C, Schneider C M and Kirschner J 1991 *Phys. Rev. Lett.* **67** 2878
[22] Reif J, Rau C and Matthias E 1993 *Phys. Rev. Lett.* **71** 1931
[23] Straub M, Vollmer R and Kirschner J 1996 *Phys. Rev. Lett.* **77** 743
[24] Thole B T, Carra P, Sette F and van der Laan G 1992 *Phys. Rev. Lett.* **68** 1943
[25] Carra P, Thole B T, Altarelli M and Wang X 1993 *Phys. Rev. Lett.* **70** 694
[26] Thomassen J, May F, Feldmann B, Wuttig M and Ibach H 1992 *Phys. Rev. Lett.* **69** 3831
[27] Li D, Freitag M, Pearson J, Qiu Z Q and Bader S D 1994 *Phys. Rev. Lett.* **72** 3112
[28] Schmitz D, Charton C, Scholl A, Carbone C and Eberhardt W 1999 *Phys. Rev.* B **59** 4327
[29] Fu C L and Freeman A J 1987 *Phys. Rev.* B **35** 925
[30] Fernando G W and Cooper B R 1988 *Phys. Rev.* B **38** 3016
[31] Kraft T, Marcus P M and Scheffler M 1994 *Phys. Rev.* B **49** 11511
[32] Asada T and Blügel S 1997 *Phys. Rev. Lett.* **79** 507
[33] Qian D, Jin X F, Barthel J, Klaua M and Kirschner J 2001 *Phys. Rev. Lett.* **87** 227204
[34] Dunn J H, Arvanitis D and Mårtensson N 1996 *Phys. Rev.* B **54** R11157
[35] Ellerbrock R D, Schatz A, Keune W and Brand R A 1995 *Phys. Rev. Lett.* **74** 3053
[36] Amemiya K, Kondoh H, Yokoyama T and Ohta T 2002 *J. Electron Spectrosc. Relat. Phenom.* **124** 151